International Journal of Environmental Science and Technology (2021) 18:2733–2746
https://doi.org/10.1007/s13762-020-03023-1

ORIGINAL PAPER

Synthesis of a novel $ZnFe_2O_4$/porous biochar magnetic composite for Th(IV) adsorption in aqueous solutions

W. D. Wang[1] · Y. X. Cui[1] · L. K. Zhang[1] · Y. M. Li[1,2] · P. Sun[1,2] · J. H. Han[1]

Received: 23 July 2020 / Revised: 22 September 2020 / Accepted: 31 October 2020 / Published online: 19 November 2020

Abstract

A novel magnetic zinc ferrite/porous biochar composite (c-PBC/ZF) was prepared and utilized to remove radioactive thorium (Th) (IV) from aqueous solutions. Zinc chloride ($ZnCl_2$) not only activates biochar during the hydrothermal synthesis of c-PBC/ZF but also serves as a basic raw material for the synthesis of zinc ferrite. In addition, nitrilotriacetic acid (NTA) plays a dual key role in catalyzing and generating large numbers of carboxyl groups (–COOH) during synthesis. The characterization results confirmed that $ZnFe_2O_4$ (ZF) particles with cubic spinel structures were successfully embedded into the porous biochar (PBC) matrix, which endowed the composite with superparamagnetism and enabled higher Th(IV) adsorption performance than that of single PBC and ZF nanoparticles. At room temperature, batch experiments showed that the removal rate of c-PBC/ZF for Th(IV) was 97.95% when the compound ratio of c-PBC/ZF was 1:1, the pH value was 4 and the adsorbent dosage was 1.2 g/L. Through the analysis of adsorption kinetics, isotherms and thermodynamics, the Th(IV) adsorption process is in good agreement with the experimental data of the quasi-second-order kinetics model and Langmuir model, indicating that the process is a spontaneous, endothermic and monolayer adsorption process. FTIR analysis verified that the main mechanism of Th(IV) removal by c-PBC/ZF was Th–O and Th(IV) complexation with a carboxyl group and a hydroxyl group. Finally, the desorption and regeneration study proved that c-PBC/ZF has a highly efficient cycling performance as an adsorbent for recovering Th(IV) from wastewater. Therefore, c-PBC/ZF is a promising adsorbent for recovering Th(IV) from wastewater.

Keywords Porous biochar · $ZnFe_2O_4$ · Magnetic composite · Thorium · Adsorption

Editorial responsibility: Fatih Şen.

✉ J. H. Han
hjhlpm@163.com

W. D. Wang
wangweida888@163.com

Y. X. Cui
1414614533@qq.com

L. K. Zhang
lkzhang@imust.cn

Y. M. Li
lymhhu@163.com

P. Sun
sp_five666@163.com

[1] School of Energy and Environment, Inner Mongolia University of Science and Technology, Baotou 014010, China

[2] School of Environmental Science and Engineering, Huazhong University of Science and Technology, Wuhan, China

Introduction

Th(IV) is a radionuclide and is generally introduced into water bodies and soils from many industrial processes, such as lignite burning in power stations, nuclear industrial radioactive waste and mining of rare earth (Li et al. 2016). Owing to its radioactivity, carcinogenicity and toxicity, effluents containing Th(IV) cause serious and irreversible environmental and biological damage. Therefore, it must be treated before discharging to the environment. Radionuclides can be removed from aqueous environments by conventional technologies, including chemical precipitation, ion exchange processes (Huang et al. 2020), electrolytic methods, adsorption (Perreault et al. 2017), membranes and reverse osmosis processes. Among these various treatment techniques, adsorption is one of the most effective techniques for the removal of Th(IV) due to its high efficiency and easy operation (Zhu et al. 2017), for which selecting a practical and affordable adsorbent is the critical step.

Biochar (Abdelhadi et al. 2017) obtained from various carbon-rich biomasses or wastes under oxygen-limited conditions and moderate temperatures is considered to be a low-cost and eco-friendly adsorbent for the remediation of various organic and inorganic contaminants in solution (Park et al. 2019). To increase the surface area of raw biochar for adsorbing contaminants, the preparation of PBC by mixing it with a precursor and activators (e.g., NaOH, KOH, $ZnCl_2$, H_3PO_4, $KHCO_3$, etc.) before pyrolysis has been investigated (Dehkhoda et al. 2015). Previous studies have suggested that chemical activation of biochar with zinc chloride can produce a biochar with a high specific surface area and a mostly microporous structure at a lower activation temperature. Although PBC exhibited a large specific surface area, abundant micropores and good sorption ability, it is difficult to separate powdered PBC from aqueous solution, which has restricted wide application to wastewater treatment (Harikishore Kumar Reddy and Lee 2014).

In recent years, magnetic separation has been introduced into the adsorbent. Various magnetic particles were employed to achieve the magnetic properties of biochar materials. The spinel ferrites MFe_2O_4 (M is a divalent metal cation such as Mn^{2+}, Mg^{2+} and Zn^{2+}) are magnetic materials that have been widely used in the treatment of wastewater (Bhowmik et al. 2019). Among ferrites, ZF is an interesting magnetic material with a large saturation magnetization, excellent chemical stability and mechanical hardness (Liu et al. 2016) that exhibited excellent adsorptive properties with the highly effective recovery during magnetic separation (Zhang Yakun Yan Liangguo 2014). Its strong Zn–O and –OH groups could provide high chemical activity to target ions (Yezi 2018). Moreover, the abundant carboxyl groups formed by the carboxylation of materials can improve the complexing capacity (Marcela et al. 2015) between the adsorbent and Th(IV), which usually leads to a large adsorption capacity(Kumar et al. 2014). Therefore, we attempted to combine PBC and ZF particles to construct a composite with high adsorption capacity and easy separation for efficient removal and recovery of Th(IV) from aqueous solution.

The primary aim of this study is to develop a novel c-PBC/ZF magnetic composite that has abundant functional groups (Metal–O, –OH and –COOH) via hydrothermal method and apply them to the removal of radioactive thorium in solution. $ZnCl_2$ not only activates biochar during the hydrothermal synthesis of c-PBC/ZF but also serves as a basic raw material for the synthesis of ZF. Moreover, NTA plays a dual key role in catalyzing hydrothermal reaction and generating large numbers of carboxyl groups during synthesis. Successful preparation of c-PBC/ZF not only overcomes the problem of porous biochar recovery but also prevents the aggregation of ZF and improves the adsorption ability of Th(IV). This study was designed to elucidate the respective roles of porous biochar and ZF and evaluate the thorium removal performance of c-PBC/ZF, which is rarely reported in the research field of using porous biochar-based composites to remove radioactive thorium from solutions. The adsorption behavior of Th(IV) was investigated through characteristic and batch adsorption experiments, and its adsorption mechanisms were further investigated. The desorption of Th(IV) and the recyclability of c-PBC/ZF were evaluated. It is of great social significance to control Th(IV) pollution and recycling the valuable nuclear energy of Th(IV). It is also of great importance to explore new ways for maize straw waste resource utilization and facilitate agriculturally sustainable development.

Materials and methods

Materials

$ZnCl_2$ (AR), ferric chloride (AR), nitrilotriacetic acid (AR), sodium hydroxide (AR level) and azo arsine III (AR level) were purchased from Tianjin No. 1 Chemical Reagent Factory. Thorium (IV) standard solution was purchased from Beijing Institute of Chemical Metallurgy, China National Nuclear Corporation. Deionized water was homemade and used in all experiments.

Preparation of c-PBC/ZF

Corn straws in the ripening stage were used as the precursor of biochar, which were collected in the rural areas around Baotou city, Inner Mongolia Autonomous Region. The corn stalks were taken back, washed, air-dried and then crushed. After 100 mesh sieving, the powder was bagged for further use.

c-PBC/ZF with different mass ratios of PBC to ZF ($m_{PBC/ZF}$) was prepared by the hydrothermal method (Wang et al. 2020). Taking the c-PBC/ZF with PBC/ZF = 1.0 for example, first, 20 g corn straw powder was taken, stirred at a macerating ratio $\left(m_{ZnCl_2} : m_{straw}\right)$ of 1.5:1 for 20 min, then soaked in a glass container for 20 h and dried at 80 °C for 24 h. Subsequently, it was pyrolyzed under a nitrogen atmosphere in a tube furnace at 600 °C for 1 h. Then, we directly put 2.41 g carbon before leaching, 5.4 g of $FeCl_3{\cdot}6H_2O$ and 4 g NTA in a beaker with 40 ml (1 + 9) HCl and stirred with a magnetic stirrer for 30 min at a constant speed (Fe/Zn = 2:1). The pH of the mixed solution was adjusted to 11 with a pH meter. The mixture was transferred to a 100-ml Teflon-lined hydrothermal synthesis reactor, followed by the hydrothermal reaction at 180 °C for 12 h. Finally, the obtained composite with $m_{PBC/ZF} = 1.0$ was washed and dried. The aforementioned method was followed to prepare c-PBC/ZF composites with $m_{PBC/ZF} = 0.2, 0.4, 0.6, 0.8, 1.2$.

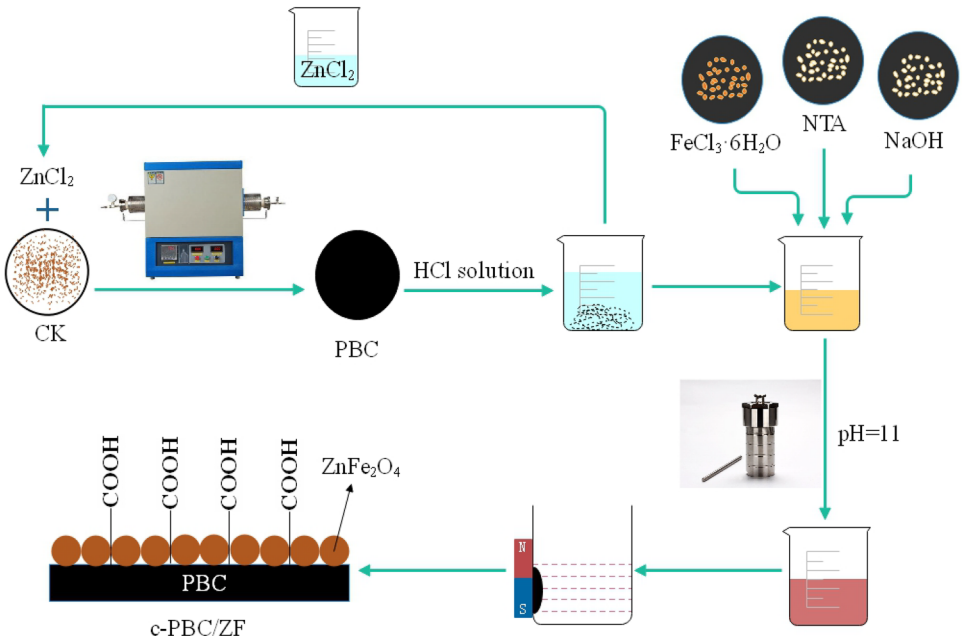

Fig. 1 Preparation process of the c-PBC/ZF

The preparation process of the c-PBC/ZF is described in Fig. 1.

Characterization of c-PBC/ZF

The morphology and element distribution of the c-PBC/ZF were observed by SEM and EDS (Hitachi s-3400n). The specific surface area and pore structure were determined by a specific surface area analyzer (NOVA4000e, Beijing Jinyi Spectrum Technology Co., Ltd.). FTIR spectrometry (Germany Bruker Tensor II type) within the range of 4000–400 cm^{-1} was used to explore the c-PBC/ZF surface functional groups and the kinds of change. The crystallinity of c-PBC/ZF was analyzed by X-ray diffraction (Bruker D8 AA25, Germany). Moreover, the magnetic properties of c-PBC/ZF and ZF were measured by a room-temperature vibrating sample magnetometer (VSM, USA).

Batch adsorption experiments

Th(IV) stock (1000 mg/L) was prepared by dissolving $Th(NO_3)_4{\cdot}4H_2O$ (purity ≥ 97%) in deionized water and further diluting it to the required concentration. The pH of the solution was maintained at 2 and was adjusted with 0.5 mol/L HNO_3. A certain concentration of ytterbium nitrate solution and an appropriate amount of c-PBC/ZF were added into an Erlenmeyer flask and placed in a constant-temperature shaker for adsorption experiments. The effects of initial pH (2.0–5.0), dosage of c-PBC/ZF (0.01–0.06 g), the complex ratios ($m_{PBC/ZF}$) (0.2–1.2), adsorption time (1 min–240 min), initial concentration (20–400 mg/L) and temperature (15–35 °C) on the adsorption performance of c-PBC/ZF were investigated by a batch experiment.

Effects of initial pH and adsorbent dosage

Adsorption experiments were performed in the conical flask with stirring at 150 rpm so as to achieve an adsorption equilibrium to study the adsorption effects of Th(IV) by c-PBC/ZF. Twenty-five milliliters of an initial concentration of 50 mg/L Th(IV) solution and a certain amount of c-PBC/ZF were added to a 150-mL conical flask. The effects of initial pH and adsorbent dose on adsorption of Th(IV) on c-PBC/ZF sample were studied over an initial pH range of 2.0–5.0 (the pH was adjusted by 0.5 mol/L HNO_3 or 0.1 mol/L NaOH solutions) and an adsorbent range of 0.01–0.06 g for 240 min at 25 °C, respectively.

Effect of $m_{PBC/ZF}$ on adsorption effect

c-PBC/ZF with different mass ratios ($m_{PBC/ZF}$ = 0.2, 0.4, 0.6, 0.8, 1.0, 1.2) was prepared by adjusting the dose of $ZnCl_2$ and PBC in the synthetic materials. And 25 mL of an initial concentration of 50 mg/L Th(IV) solution and 0.05 g of c-PBC/ZF with different mixing ratios were added to a 150-mL conical flask. Then, the flask was placed in a constant-temperature oscillator with a temperature of 25 °C and a rotation speed of 150 r/min to perform an adsorption reaction for 240 min at pH = 4.0.

Sorption kinetics

0.05 g as-prepared c-PBC/ZF with different $m_{PBC/ZF}$ was added to 150-mL conical flasks with 25 mL Th(IV) solution of 50 mg/L. Then, the flasks were placed in a constant-temperature oscillator with a temperature of 25 °C and a rotation speed of 150 r/min to perform an adsorption reaction at pH = 4.0, and aliquots were sampled at different time intervals (1–240 min).

Adsorption isotherms

0.03 g of c-PBC/ZF was added to a 150-mL conical flask. Then, the flask was placed in a constant-temperature oscillator to perform an adsorption reaction at pH = 4.0. Twenty-five milliliters of Th(IV) solutions with different initial concentrations (20–400 mg/L) was selected and oscillated with a rotation speed of 150 r/min for 240 min at 15 °C, 25 °C and 35 °C, respectively.

After adsorption, the mixtures were filtered by 0.22-mm filters and then the concentration of Th(IV) ions was analyzed by an atomic absorption spectrophotometer (PE-AA800) using the azo three spectrophotometry at λ = 660 nm. All tests were repeated, and the results were averaged. Equations (1) and (2), respectively, represent the removal rate R and adsorption quantity q_e of Th(IV) by c-PBC/ZF.

$$R = \frac{(C_0 - C_e)}{C_e} \times 100\% \tag{1}$$

$$q_e = \frac{(C_0 - C_e)V}{m} \tag{2}$$

where q_e is the equilibrium adsorption capacity, mg/g; C_0 and C_e are the mass concentration of Th(IV) in the solution at the initial time and the equilibrium time, respectively, mg/L. R is the removal rate of Th(IV), %; V is the volume of the solution, L; m is the dosage of adsorbent, g.

Desorption and recycling

The desorption and recycling study of c-PBC/ZF was carried out for six consecutive adsorption cycles at 25 °C and pH = 4.0. 25 mL of 50 mg L^{-1} Th(IV) solutions was adsorbed first by 30 mg of adsorbent for 4 h in each cycle. Afterward, it was separated by a magnet from the treated solution and regenerated by 25 mL of 0.5 mol L^{-1} citric acid for 6 h, followed by washing with deionized water and again deionized water and then dried at 105 °C. c-PBC/ZF recovered and regenerated was employed for the next five cycle under the same experimental and regeneration methods. The recovery (r) of Th(IV) in the solid phase was calculated.

$$r(\%) = \frac{m_{des}}{m_{ads}} \times 100 \tag{3}$$

m_{des} and m_{ads} are the release amount of Th(IV) in aqueous solution and the adsorption amount of Th(IV) on adsorbent (mg/L), respectively.

Results and discussion

Characterization

SEM

To clearly and intuitively reflect the morphological changes of the c-PBC/ZF composite and reveal the distribution of ZF particles on the PBC surface, SEM images of PBC and ZF particles, SEM images and EDS spectra of the c-PBC/ZF are presented in Fig. 2. According to the previous work done by our research group, the typical biochar morphology of corn straw powder after direct carbonization is porous structure with smooth surface and no impurities (Zhang et al. 2019). The unmodified pure BC has an abundant pore structure, which is conducive to Th(IV) adsorption. However, as shown in Fig. 2a, biochar modified by $ZnCl_2$ not only produces a large number of micropores, but also expands the existing micropores into mesopores. $ZnCl_2$ plays a skeleton role in the process of carbonization and activation. PBC with huge specific surface area is formed when $ZnCl_2$ is washed with ionized water. Therefore, the specific surface area of PBC modified by $ZnCl_2$ increased by more than ten times compared with that of BC (Table 1), which greatly improved its adsorption performance. In addition, as shown in Fig. 2b, it can be clearly seen that the pure ZF particles exist as octahedral architectures, which consist of eight well-defined (111) crystal planes. Individual ZF particles aggregate together to form nanoclusters. In comparison, the octahedral ZF particles for c-PBC/ZF were uniformly dispersed and loaded onto the surface of PBC as in Fig. 2c. It can be seen that PBC effectively prevents the agglomeration of ZF particles and ensures that c-PBC/ZF still has a large surface area. Moreover, The agglomeration between the particles is greatly reduced, possibly because that the interaction component between the two prohibits the agglomeration of ZF particles. The relative contents of the main elements in c-PBC/ZF can be qualitatively reflected by element mapping. As seen from Fig. 2d, e, f and g, the main elements of the composite material include, in order of decreasing content, C, O, Fe and Zn. The corresponding EDS spectrum (Fig. 2h) confirms the existence of Zn, Fe, and O, and the atomic ratio of Zn to Fe

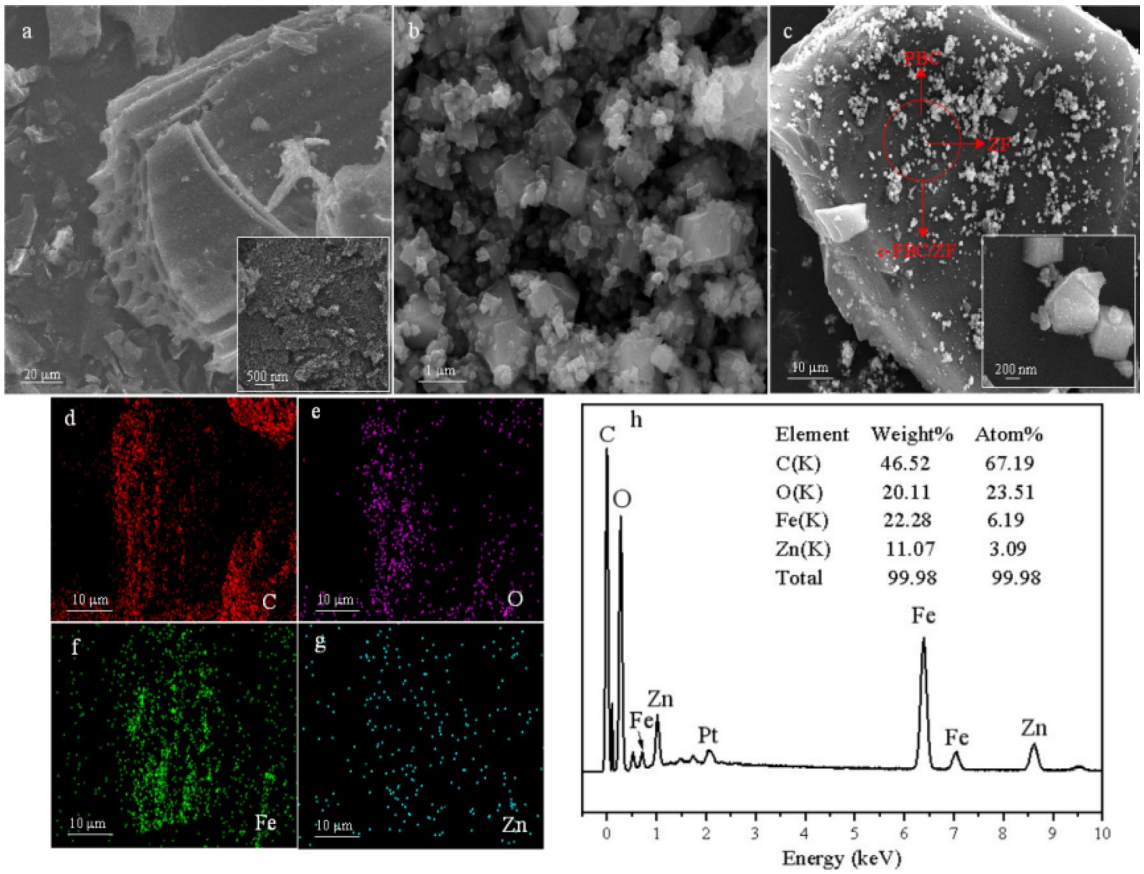

Fig. 2 FE-SEM images of PBC (**a**), ZF (**b**), c-PBC/ZF composite (**c**) and EDS analysis of c-PBC/ZF: carbon (**d**), oxygen (**e**), iron (**f**), zinc (**g**), EDS spectrum (**h**)

Table 1 Analysis of specific surface area of carbon materials

	Specific surface area ($m^2 \cdot g^{-1}$)	Pore volume ($cm^3 \cdot g^{-1}$)	Pore size (nm)
BC	79	0.58	4.39
PBC	1047	0.49	3.68
c-PBC/ZF	523	0.32	3.29

was close to 1:2, which supports the stoichiometric composition of ZF. Meanwhile, the peak of C confirmed the existence of PBC, while the peak of O was attributed to the presence of ZF and oxygen-containing functional groups on c-PBC/ZF. All these facts indicate that ZF particles have been successfully loaded onto PBC.

BET analysis

The specific surface area of carbon materials prepared in this experiment is shown in Table 1. According to BET analysis, the specific surface area of PBC was 1147 $m^2 \cdot g^{-1}$, which is 13.52 times that of BC. Obviously, the specific surface area of PBC was much larger than that of BC, which could be attributed to the reaction between zinc chloride and the organic components of the biomass that promoted the development of the pore structure. At the same time, the large number of mesopores generated by the material increased the specific surface area of the composite. Therefore, the physical adsorption effect of Th(IV) on the composite material was significantly improved. The pore volume and pore diameter of PBC were significantly reduced compared with those of BC. The pore structure of pure BC was mainly macroporous and mesoporous, while the PBC modified by $ZnCl_2$ had an increased proportion and number of mesopores. This may also be due to the reaction between $ZnCl_2$ and organic matter in the straw to further promote the development of the pore structure of biochar. At the same time, many new unsaturated bonds and oxygen-containing functional groups were introduced. The magnetic composite material synthesized in this study showed excellent physical and chemical adsorption properties for Th(IV) in wastewater, which is consistent with the SEM results. In addition, BET test results showed that the

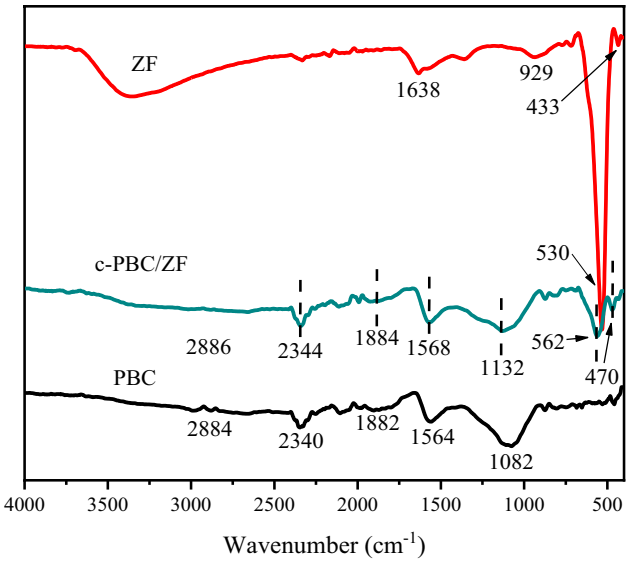

Fig. 3 FTIR images of PBC, ZF and c-PBC/ZF

specific surface area of c-PBC/ZF was 523 $m^2 \cdot g^{-1}$, which is much larger than that of pure biochar (79 $m^2 \cdot g^{-1}$) and smaller than that of PBC. Its PV and PS were slightly lower than those of PBC because ZF particles will occupy space in the pores of PBC and cause a small number of micropores to be blocked when successfully embedded into PBC. The high specific surface area of c-PBC/ZF provides more adsorption sites and reaction centers for Th(IV) adsorption, which is one of the reasons for the excellent removal effect of Th(IV).

FTIR analysis

Figure 3 shows the infrared spectra of ZF, PBC and c-PBC/ZF recorded in 4000–400 cm^{-1}. As seen from the FTIR spectrum of ZF, the tensile vibrations of Fe–O and Zn–O occurred at 530 cm^{-1} and 433 cm^{-1}, respectively, corresponding to M–O at octahedral and tetrahedral positions in the spinel structure (Ghobadi et al. 2018; Liang et al. 2020). The peak width of the ZF sample at 929 cm^{-1} corresponds to bending of the hydroxyl moiety (–OH) (Yang et al. 2017). The characteristic absorption peak at 1638 cm^{-1} corresponds to stretching of the carboxyl group (–COOH) (Xiong et al. 2019), indicating that the addition of NTA to the prepared material can successfully lead to carboxylation. This provides very favorable conditions for the chemisorption of Th(IV) by c-PBC/ZF. The FTIR spectra of PBC showed peaks at 1882 cm^{-1} and 2884 cm^{-1}, corresponding to oxygen-containing functional groups such as hydroxyl-associated C=O and C–O–C, respectively. The peaks at 1564 cm^{-1} and 2340 cm^{-1} are attributed to the presence of unsaturated bonds such as C≡C and C=C. This could be attributed to a variety of active groups generated by the reaction between $ZnCl_2$ and straw organic components during the activation of PBC, which also indicates that PBC not only has a strong physical adsorption capacity for Th(VI) but also has the chemical property of complexing with Th(VI). It can be seen that the FTIR spectra of c-PBC/ZF has all the major absorption peaks of ZF and PBC, indicating that zinc ferrite nanoparticles have been successfully embedded into the PBC matrix.

XRD analysis

The crystal structure and phase composition of the samples were analyzed by XRD. Figure 4 shows the XRD patterns of PBC, ZF and c-PBC/ZF. Obviously, there are many impurity peaks in all XRD patterns of PBC. A strong and wide peak centered at 23° corresponds to the crystal surface of a typical disordered glassy carbon polymer, which represents the typical diffraction pattern of amorphous carbon. The XRD pattern of ZF was completely consistent with the cubic spinel structure (Somvanshi et al. 2020) (JPCDS 1-1109), and no characteristic peaks of impurities were found. Evidence of the expected spinel ferrite structure was found in the XRD pattern of c-PBC/ZF, which proved the existence of ZF in c-PBC/ZF. In addition, it can be seen from Fig. 4 that the XRD patterns of ZF and the c-PBC/ZF samples are similar, and the observed peaks and strong peaks indicate that the crystallinity of the ZF samples is good. ZF shows seven main characteristic peaks at $2\theta = 18.52°$, 30.01°, 35.01°, 42.91°, 53.12°, 56.58° and 63.29°, corresponding to the spinel structures on the crystal planes of (111), (220), (311), (400), (422), (511) and

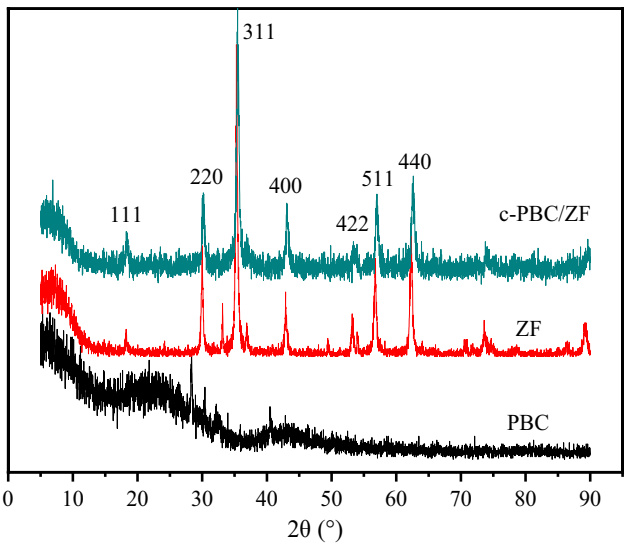

Fig. 4 XRD images of PBC, ZF and c-PBC/ZF

(440), respectively. It is also confirmed by FTIR analysis that the two main absorption peaks corresponding to the cubic spinel structure of ZF are located at 562 cm^{-1} and 470 cm^{-1}. The main characteristic diffraction peaks were similar to those of ZF when ZF was successfully embedded into PBC. The XRD peak of c-PBC/ZF at nearly 23° is not obvious, which may be because the diffraction intensity of PBC is small and relatively low. These structural properties provide for the magnetic separability of c-PBC/ZF.

Hysteresis loop analysis

To further determine the magnetic properties of c-PBC/ZF composite, vibrating sample magnetometer (VSM) was used to study the magnetic properties of the ZF and c-PBC/ZF under applied field of 10 kOe. The characteristics of magnetization curve determine the practicability of ferromagnetic materials. The hysteresis loop of ZF and c-PBC/ZF obtained in the experiment is shown in Fig. 5. The obtained curve shows the normal narrow hysteresis loop (S shape). Coercive force (H_C) is approximately zero at room temperature. It can be attributed to superparamagnetic behavior, which does not leave a residual magnetic moment when the magnetic field is removed(Sun 2006), which contributes to easy and rapid magnetic separation. The saturation magnetization of ZF and c-PBC/ZF is 45.48 emu·g^{-1} and 18.85 emu·g^{-1}, respectively. The saturation magnetization (Ms) of c-PBC/ZF is slightly lower than that of ZF due to the presence of the nonmagnetic component PBC (Mahmed et al. 2014). As shown in photographs of c-PBC/ZF, the magnetic properties are conducive to the rapid separation of c-PBC/ZF from aqueous solution. These results indicated that c-PBC/ZF has excellent magnetic properties and is conducive to adsorption separation and desorption regeneration. Therefore, an external magnetic field can be used to separate and recycle c-PBC/ZF to achieve the effect of recycling and greatly reduce energy consumption during the Th(IV) adsorption and extraction process.

Adsorption performance

Effect of solution pH

For the chemical adsorption process of c-PBC/ZF, the initial pH value of the solution plays a vital role in the study of the adsorption process. The change in pH directly affects the surface charge of c-PBC/ZF, the formation of adsorption sites, the chemical interaction between c-PBC/ZF and metal ions and the chemical form of the adsorbate. Figure 6 shows the experimental results of the effect of initial pH on Th(IV) adsorption by c-PBC/ZF. It can be seen from the figure that in acidic solution, the adsorption amount of Th(IV) by c-PBC/ZF increased with increasing pH value. However, the adsorption amount decreased gradually with increasing pH value when pH < 4.0. This could indicate that the surface of c-PBC/ZF is covered with highly protonated hydrogen at lower pH. As seen from the morphological distribution of Th(IV) at different pH values, at low pH, the main morphologies of Th(IV) are Th^{4+} and $Th(OH)^{3+}$ due to inhibition of hydrolysis. They compete with H_3O^+ on the surface of c-PBC/ZF for active sites on the surface of the adsorbent,

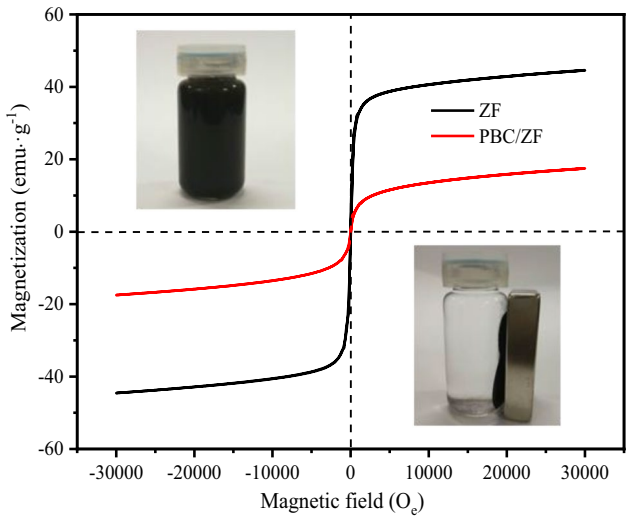

Fig. 5 Magnetic hysteresis curves of ZF and c-PBC/ZF composite at room temperature and photographs of c-PBC/ZF composite dispersed into solution and magnetic separation by an ordinary magnet after 5 s

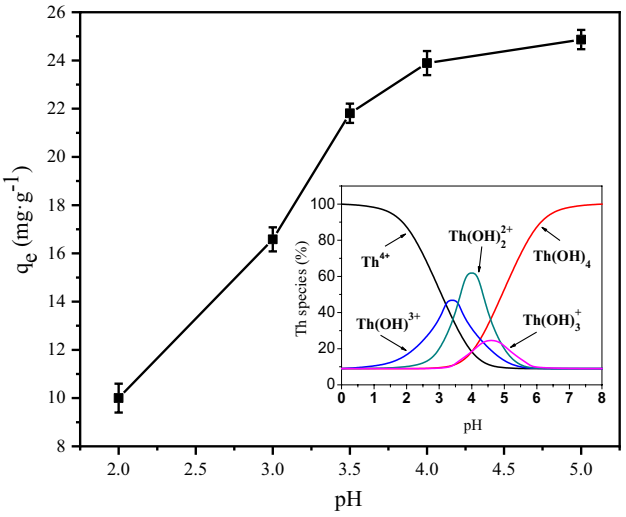

Fig. 6 Effect of pH on Th(IV) adsorption onto c-PBC/ZF and the speciation of Th(IV) in aqueous solution. Conditions: C_0(Th(IV)) = 50 mg/L, V = 25 ml, c-PBC/ZF dose = 2.0 g/L, temperature = 25 °C and t = 240 min

resulting in a lower adsorption of c-PBC/ZF. However, the concentration of H_3O^+ decreases with increasing pH, and the adsorption capacity gradually increases. Th(IV) mainly exists in the form of $Th(OH)_2^{2+}$ and $Th_2(OH)_2^{6+}$ when the pH is 4.0. In contrast, the positive surface charge of the adsorbent decreases with increasing pH and the repulsive force of Th(IV) decreases, which makes $Th(OH)_2^{2+}$ and $Th_2(OH)_2^{6+}$ more easily adsorbed than Th^{4+} (Xu et al. 2015). At the same time, the complexation of active groups such as the carboxyl group and hydroxyl group of c-PBC/ZF and the hydrolyzed product of Th(IV) is enhanced. The internal electrostatic and hydrogen bonding effects of c-PBC/ZF are destroyed when pH > 4.0. What's more, Th(IV) formed $Th(OH)_4$ precipitation ($Ksp = 2 \times 10^{-45}$) in the solution when pH > was 4.0 and $ThO(OH)_2$ ($Ksp = 5 \times 10^{-24}$) and ThO_2 precipitation could be formed after losing 1 or 2 water molecules, which causes false adsorption. Therefore, the adsorption amount of Th(IV) by c-PBC/ZF is still increasing. In summary, the pH value of the solution was controlled at 4.0 in subsequent tests to reduce the impact of pH on the tests. To the best of our knowledge, c-PBC/ZF showing effective Th(IV) capture under such conditions is never reported in the literature(Wang et al. 2019).

Effect of c-PBC/ZF dosage on adsorption effect

Obviously, the removal rate of Th(IV) by c-PBC/ZF increased sharply with increasing adsorbent dose at the initial stage of adsorption as shown in Fig. 7. However, its removal rate of Th(IV) almost reached a constant value when the dose exceeded 0.03 g. The trend is to be expected because the high amount of adsorbent makes the effective solute insufficient to completely cover the c-PBC/ZF removal site. However, the equilibrium adsorption amount of c-PBC/ZF gradually decreased, which is mainly due to the increase in the amount of unused active sites on the adsorbent in a certain concentration of Th(IV) solution. The aggregation and overlap of the active centers reduced the c-PBC/ZF adsorbent specific surface area (Oter and Zorer 2020) so that the adsorption amount of Th(IV) on c-PBC/ZF in the aqueous solution decreased. It can be observed from the figure that the maximum removal rate of Th(IV) by c-PBC/ZF is 97.95% when the dose reaches 1.2 g/L. Therefore, 1.2 g/L was the optimal dose of adsorbent.

Effect of different complex ratios ($m_{PBC/ZF}$)

The mass ratios of PBC and ZF ($m_{PBC/ZF}$) will directly affect the specific surface area, ratio of active groups and magnetic properties of the synthesized composite materials. Therefore, $m_{PBC/ZF}$ is an important factor to investigate the adsorption effect of c-PBC/ZF on Th(IV). Figure 8 shows the effect of c-PBC/ZF with different $m_{PBC/ZF}$ on Th(IV) adsorption. The removal rate and adsorption amount are the smallest when the compound ratio is 0.2. The adsorption rate of Th(IV) by c-PBC/ZF gradually increased when the compound ratio was 0.4–1.0, and both exceeded 87%. The removal rate and adsorption capacity of Th(IV) by c-PBC/ZF increased significantly with a further increase in the compound ratio to 1.2, which may be caused by excessive PBC not compounded with ZF (Shen et al. 2015), and its magnetic separation capacity also decreased. Therefore, c-PBC/ZF with a combined ratio of 1.0 had the best adsorption effect on Th(IV) in the wastewater. The combined ratio of 1.0 was selected as c-PBC/ZF in the following tests.

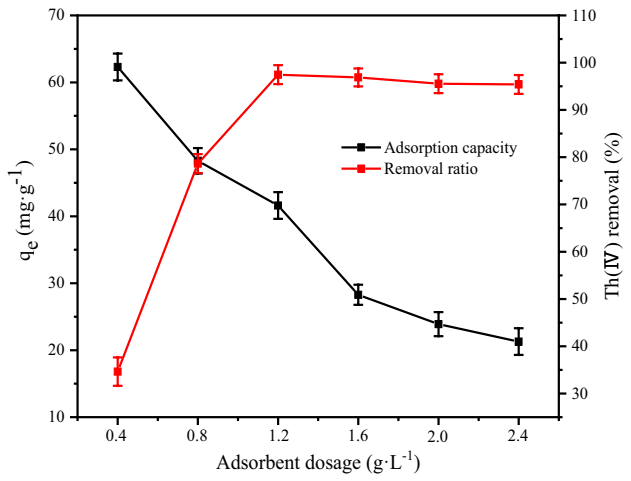

Fig. 7 Effect of dosage on Th(IV) adsorption onto c-PBC/ZF. Conditions: C_0(Th(IV)) = 50 mg/L, V = 25 ml, pH = 4.0, temperature = 25 °C and t = 240 min

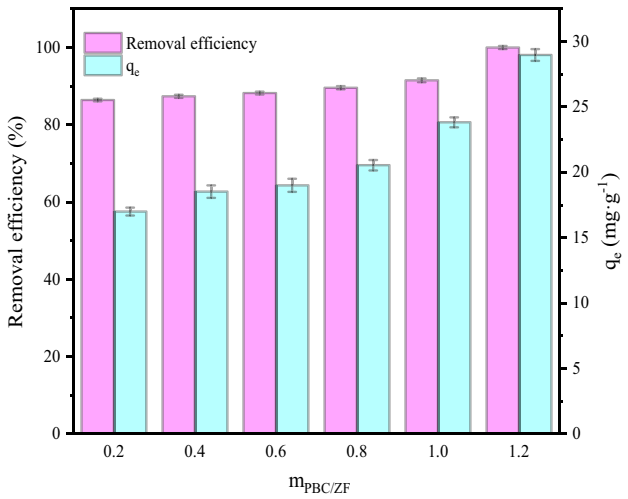

Fig. 8 Effect of $m_{PBC/ZF}$ on Th(IV) adsorption onto the c-PBC/ZF. Conditions: C_0(Th(IV)) = 50 mg/L, V = 25 ml, c-PBC/ZF dose = 2.0 g/L, pH = 4.0, temperature = 25 °C and t = 240 min

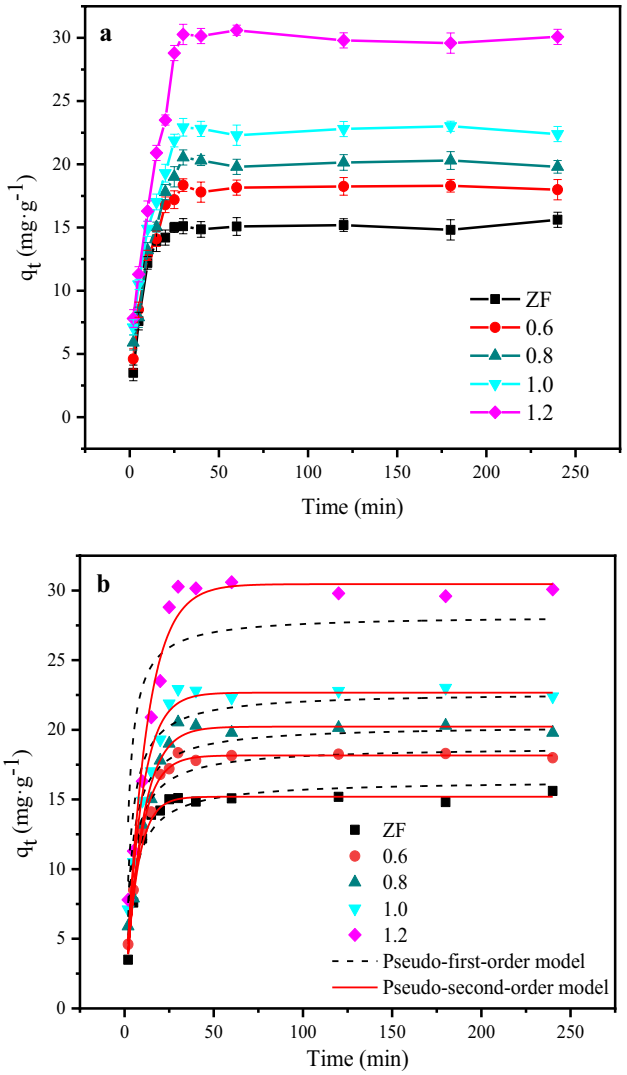

Fig. 9 Adsorption kinetics (**a**) and its mechanism (**b**) of c-PBC/ZF. Conditions: C_0(Th(IV)) = 50 mg/L, V = 25 ml, c-PBC/ZF dose = 2.0 g/L, pH = 4.0 and temperature = 25 °C

Effect of time and different complex ratios ($m_{PBC/ZF}$): adsorption kinetics

The adsorption properties of Th(IV) by c-PBC/ZF were investigated from the perspective of adsorption kinetics. The adsorption kinetics of c-PBC/ZF with different $m_{PBC/ZF}$ are presented in Fig. 9a. It can be seen that the adsorption process is time dependent, the equilibrium absorption capacity and adsorption rate of c-PBC/ZF increase simultaneously with the raise of $m_{PBC/ZF}$. The adsorption capacity of c-PBC/ZF to Th(IV) units increased rapidly in the first 20 min. The rapid adsorption at this stage could be attributed to nano-sized $ZnFe_2O_4$, which facilitates the diffusion of Th(IV) from the aqueous solution to the active site of the adsorbent (Zhang et al. 2018). In addition, c-PBC/ZF could provide more adsorption sites at the beginning, and the concentration of Th(IV) in the solution was higher. Moreover, the driving force for mass transfer was also larger, leading to a higher growth rate of the early adsorption amount. The adsorption entered the stage of slow diffusion after 20 min. The number of active sites gradually decreased with increasing reaction time. The growth rate of the c-PBC/ZF unit adsorption capacity gradually slowed until the adsorption reached equilibrium after 30 min. After that, the reaction process entered the adsorption equilibrium stage. It is also noted that the adsorption capacity of c-PBC/ZF is higher than that of ZF, indicating the superior adsorption performance of PBC. However, compared to c-PBC/ZF with other $m_{PBC/ZF}$, the adsorption capacity of c-PBC/ZF with $m_{PBC/ZF} = 1.2$ is much higher, which may be caused by the superfluous PBC that does not compound with ZF. This is consistent with the results obtained in "Effect of different complex ratios ($m_{PBC/ZF}$)" section. These facts suggests that the resultant c-PBC/ZF might has highly potential applications for the adsorption of Th(IV).

To further study the adsorption rate of Th(IV) by c-PBC/ZF and its influencing factors and the possible mechanism to explain the reaction rate law, the obtained experimental data were fitted with quasi-first-order and quasi-second-order kinetic models (He et al. 2019), and the equations are shown in Eqs. (3) and (4).

Quasi first order dynamic equation:

$$q_t = q_e\left[1 - \exp\left(-\frac{k_1}{20303}t\right)\right] \tag{4}$$

Quasi second order dynamic equation (Benguella and Benaissa):

$$q_t = -\frac{k_2 q_e^2 t}{1 + k_2 q_e t} \tag{5}$$

where q_t is the adsorption capacity (mg·g^{-1}) of Th(IV) by c-PBC/ZF at time; q_e is the adsorption capacity of c-PBC/ZF to Th(IV) at equilibrium (mg·g^{-1}); t is reaction time (min^{-1}); K_1 is the first-order adsorption rate constant (min^{-1}). K_2 is the secondary adsorption rate constant [g·(mg·min)$^{-1}$].

Dynamic data of different concentrations were fitted, and the results of nonlinear fitting are shown in Fig. 9b. The parameters of the quasi-first-order and quasi-second-order dynamic models are shown in Table 2. The degree of conformity of the two models can be tested by the linear correlation coefficient R^2(dos Santos et al. 2019). Table 2 shows that the correlation coefficient R^2 of the quasi-secondary kinetic model is higher than that of the quasi-primary model. The theoretical equilibrium adsorption capacity calculated by the model is approximately the same as the experimental value, indicating that the adsorption of Th(IV) by c-PBC/ZF is more in line with the quasi-secondary kinetics. Therefore,

Table 2 Adsorption kinetics data of Th(IV) by c-PBC/ZF

$m_{PBC/ZF}$	Q_e (mg·g^{-1})	Quasi first order dynamic model			Quasi second order dynamic model		
		Q_t (mg·g^{-1})	k_1 (min^{-1})	R^2	Q_t (mg·g^{-1})	k_2 (g·mg^{-1} min^{-1})	R^2
0	15.101	16.370	0.234	0.931	15.199	0.148	0.992
0.6	18.353	18.778	0.270	0.928	18.162	0.121	0.988
0.8	20.542	20.306	0.297	0.872	20.227	0.107	0.972
1.0	22.931	22.677	0.336	0.876	22.669	0.114	0.959
1.2	30.272	28.204	0.451	0.700	30.457	0.087	0.964

the mechanism of c-PBC/ZF adsorption of Th(IV) is based on chemical reaction or chemical adsorption(Huang et al. 2019; Sun et al. 2018).

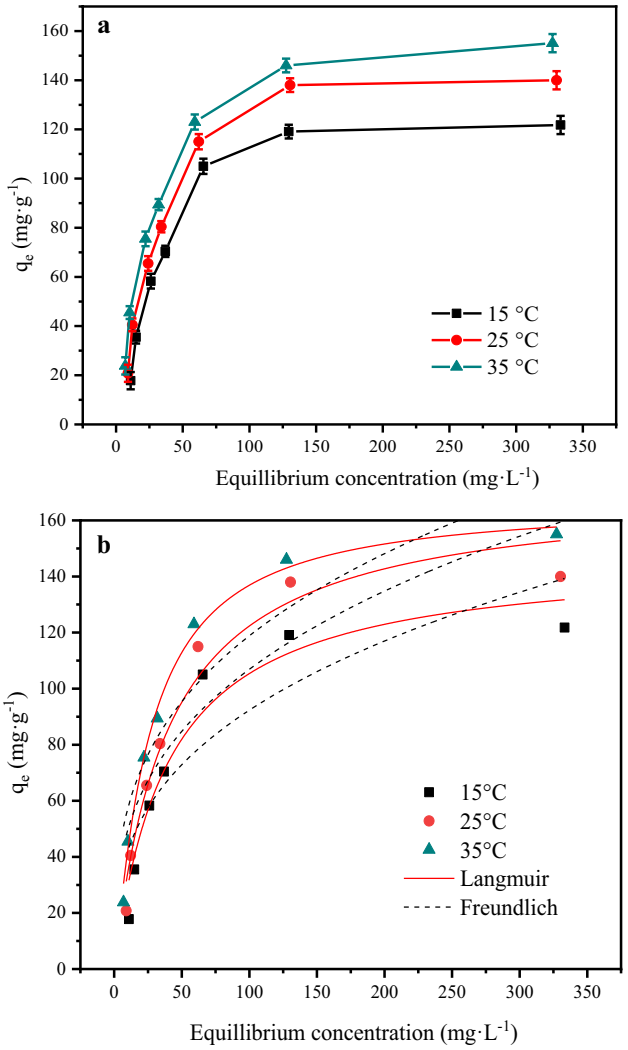

Fig. 10 The adsorption isotherm curves of c-PBC/ZF (**a**) and Langmuir, Freundlich plot to estimate the adsorption properties of c-PBC/ZF (**b**). Conditions: V = 25 ml, c-PBC/ZF dose = 1.2 g/L, pH = 4.0, temperatures = 15–35 °C and t = 240 min

Effect of initial Th(IV) concentration and temperature: adsorption isotherms

It can be seen from Fig. 10a that the adsorption amount of c-PBC/ZF to Th(IV) increases with the increase in the initial concentration of Th(IV) until the adsorption capacity is reached. It could be attributed to the increase in the amount of Th(IV) in the solution as the initial concentration of Th(IV) increases(Li et al. 2015). Then, the active sites on the c-PBC/ZF surface are gradually adsorbed to saturation so that the amount of adsorption increases. At the same time, the adsorption capacity of c-PBC/ZF for Th(IV) increased significantly with increasing temperature, indicating that the increase in temperature was conducive to the adsorption of Th(IV). Moreover, at 35 °C, the equilibrium adsorption capacity of c-PBC/ZF for Th(IV) was 155.08 mg/g. It may be that the number of active sites of the c-PBC/ZF surface that can interact with Th(IV) increases with increasing temperature. As a result, the adsorption effect is improved. To describe the adsorption mechanism of Th(IV) on c-PBC/ZF more accurately, the Langmuir adsorption isothermal model (Mohammadi et al. 2020) and Freundlich adsorption isothermal model(Jung et al. 2017) were used to fit the experimental data obtained at 15, 25 and 35 °C. The fitting formulas are shown in Eqs. (6) and (7).

$$\text{Langmuir}: q_e = \frac{K_L q_m}{1 + K_L C_e} C_e \tag{6}$$

$$\text{Freundlich}: q_e = K_F C_e^{1/n} \tag{7}$$

where C_e is the concentration of Th(IV) in the solution at adsorption equilibrium, mg·L^{-1}; q_e is the equilibrium adsorption capacity, mg•g^{-1}; q_m is the saturated adsorption capacity, mg•g^{-1}; K_L is the Langmuir constant, L•mg^{-1}; K_F is the constant representing the adsorption capacity, L•g^{-1}; and n is the constant of the adsorption trend.

C_e was used to plot q_e and fit the curve, and the specific parameters and fitting results are shown in Table 3 and Fig. 10b. By comparing the fitting curves of the two isotherm equations in Fig. 10b and combining Table 3, it

Table 3 Th(IV) adsorption isotherm data of c-PBC/ZF

Temperature/°C	Langmuir			Freundlich		
	Q_m (mg·g^{-1})	K_L (L·mg^{-1})	R^2	1/n	K_F (mg^{1-n}g^{-1}·L^{-n})	R^2
15	42.315	0.189	0.947	0.341	19.144	0.752
25	42.273	0.212	0.966	0.334	22.918	0.791
35	41.593	0.223	0.992	0.318	27.486	0.832

can be seen that the Langmuir adsorption curve fits better than the Freundlich adsorption curve under different temperature conditions. The theoretical adsorption capacity Q_{max} obtained at the same time is basically consistent with the experimental value. Therefore, the Langmuir equation was used to describe the adsorption dynamics of Th(IV) by c-PBC/ZF, which was better than the Freundlich equation. In other words, the adsorption process of Th(IV) by c-PBC/ZF is more consistent with the single-layer adsorption mode, and the surface active sites are uniformly distributed. It is mainly uniformly adsorbed.

The K_L value of the parameter increases with increasing temperature in the Langmuir model, indicating that the adsorption of Th(IV) on c-PBC/ZF is an endothermic process (Vergis et al. 2019). The increase in temperature is more conducive to the occurrence of the adsorption reaction.

In addition, the separation factor constant R_L is often used to test whether the composite material is suitable for the adsorption of some metal ions. The value of R_L can be calculated according to Eq. (8). $R_L > 1.0$ indicates that c-PBC/ZF is not suitable for adsorbing the metal ion; $0 < R_L < 1.0$ indicates that c-PBC/ZF is suitable for adsorbing the metal ions; $R_L = 0$ means that the adsorption reaction is irreversible.

$$R_L = \frac{1}{1 + K_L C_0} \tag{8}$$

where K_L is Langmuir equilibrium adsorption constant (L/mg) and C_0 is the initial concentration (mg·L^{-1}).

After calculation, the R_L values obtained at different temperatures and concentrations were between 0.009 and 0.15, indicating that c-PBC/ZF composite is suitable for Th(IV) adsorption in wastewater.

Adsorption thermodynamics

The Van't Hoff equation was used to analyze the adsorption thermodynamics of the reaction according to the adsorption isotherm data at different temperatures. The relevant calculation results are shown in Table 4.

As shown in Table 4, the ΔH values of the adsorption reactions are all positive, indicating that the reaction process is an endothermic reaction. These results combined with the results of the adsorption isotherm indicate that the adsorption amount of c-PBC/ZF to Th(IV) increases with increasing temperature. The experimental results are consistent with the theoretical verification. The degrees of freedom of the entire system increase when $\Delta S > 0$ of the reaction, which is attributed to the interaction between the adsorption site and Th(IV). Furthermore, the number of free ions is increased, which makes the whole system more disordered. $\Delta G < 0$ indicates the spontaneity of the adsorption process.

Analysis of adsorption mechanism

In order to further study the adsorption mechanism of Th(VI) by c-PBC/ZF composite, FTIR spectroscopy was used to analyze the changes of surface functional groups before and after Th(VI) adsorption by c-PBC/ZF composite, as shown in Fig. 11a. The results showed that the main adsorption peaks of c-PBC/ZF were similar to those after Th(VI) adsorption. The peaks attributed to Fe–O and Zn–O of c-PBC/ZF were shifted from 562 cm^{-1} and 470 cm^{-1} to 580 cm^{-1} and 442 cm^{-1} after Th(VI) adsorption. The peak intensity, amplitude and width decreased. It was proven that the M–O bond participated in the binding of target ions and played an important role in the process of Th(VI) adsorption (Zhang et al. 2014). In addition, the absorption peaks of the oxygen-containing carboxylic acid C=O, C–O–C and

Table 4 The adsorption thermodynamic parameters of Th(IV) by c-PBC/ZF composite

C_0 (mg·L^{-1})	ΔH (kJ·mol^{-1})	ΔS (J·mol^{-1} K^{-1})	ΔG (kJ·mol^{-1})		
			15 °C	25 °C	35 °C
30	4.19	67.43	− 17.50	− 18.51	− 19.50
50	4.12	66.04	− 15.49	− 16.56	− 17.79
80	3.88	64.85	− 14.49	− 15.49	− 16.42
100	2.87	62.51	− 13.62	− 14.62	− 15.52
200	1.45	48.67	− 14.49	− 13.85	− 14.49

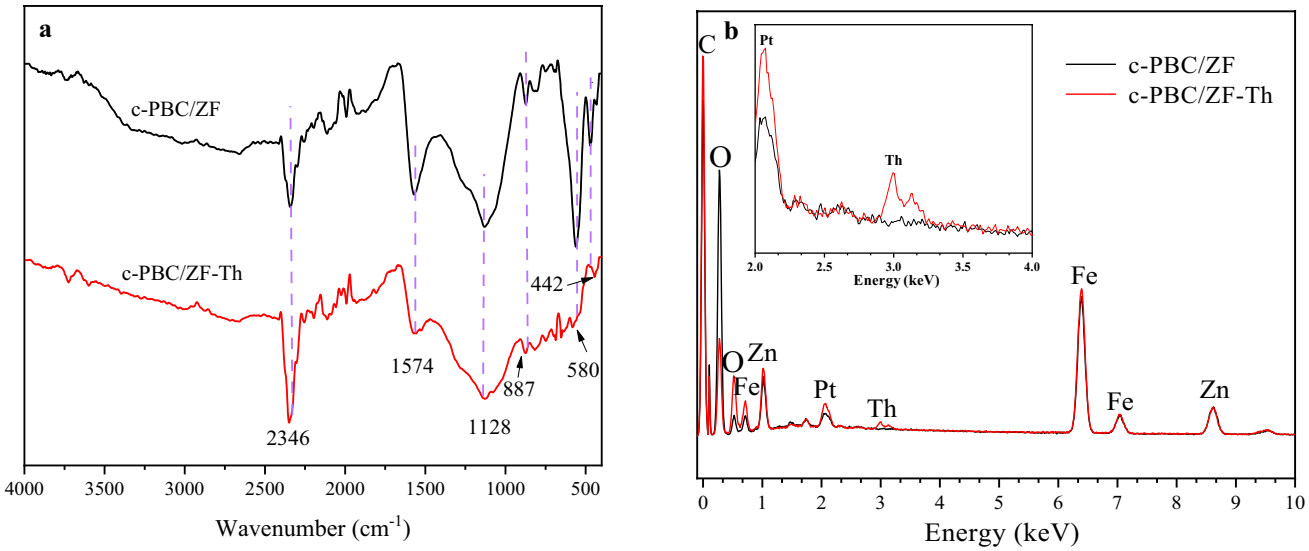

Fig. 11 FTIR (**a**), EDS (**b**) spectrum of c-PBC/ZF and Th(IV)-loaded c-PBC/ZF

associated hydroxyl–OH functional groups on the c-PBC/ZF composite shifted from 1132 and 873 cm^{-1} to 1128 and 887 cm^{-1}, respectively. This may be due to their complexation with Th(VI) and the formation of Th–O bonds, among which a large number of carboxyl groups play a very important role in the complexation of Th(VI) (Xu et al. 2015). The surface of the synthesized c-PBC/ZF has typical Lewis basic groups, such as CH_3COO^- and hydroxyl–OH, according to soft and hard acid and base theory. It is difficult to deform, has a tight combination of electrons and has low polarizability. Therefore, it is a hard alkali substance. However, the ratio of the charge density to the ion radius of Th(VI) ions is large, and the polarization rate is low, making it a "hard acid." c-PBC/ZF easily forms a stable complex with the empty orbital of Th(VI) in solution through coordination when other factors are the same. There is a lone pair center on active groups such as CH_3COO^-, –OH of c-PBC/ZF. Therefore, "hard base" substances and "hard acid" substances can react quickly to form stronger bonds and generate more stable complexes (Kokalj 2012). The aromatic C=C peak at 2340 cm^{-1} and the C≡C peak at 1568 cm^{-1} in the spectrum of c-PBC/ZF are shifted, and the peak strength is changed, indicating that these olefins, alkynes and aromatics are complexed with Th(VI) by bond electrons as ligands.

In addition, the EDS analysis in Fig. 11b shows that a Th(VI) diffraction peak appears on the c-PBC/ZF surface after adsorption by comparing the element composition of the c-PBC/ZF surface before and after adsorption. At the same time, the peak intensity is higher, and the peak width is larger. This shows that a large amount of Th(VI) is adsorbed on the c-PBC/ZF surface. This is consistent with the results of FTIR spectral analysis in this section.

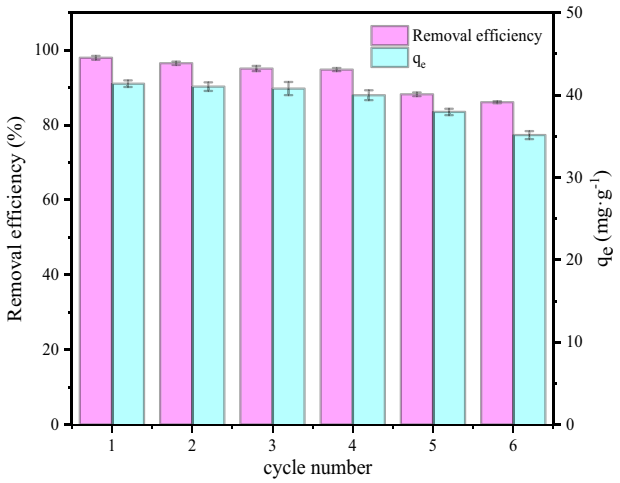

Fig. 12 Regeneration of c-PBC/ZF in the removal of Th(VI)

Desorption and reutilization

In practice, the choice of adsorbent depends not only on its ability to absorb heavy metals but also on the economic efficiency of its regeneration and reuse. To evaluate the reusability of c-PBC/ZF and realize the recovery of Th(IV) in wastewater, Th(IV) was measured from adsorbed Th(IV) to desorbed c-PBC/ZF in this study. Figure 12 shows the washing of citric acid processing of regenerated adsorbents after six cycles of adsorption. The regeneration investigation was carried out in six consecutively adsorption–desorption cycles to evaluate removal efficiencies in each cycle, respectively. The resolution rate of the adsorbent reached above 90% in the first four cycles. The resolutions were 88.21%

and 86.08% in the fifth and sixth cycles, respectively, and may gradually decline thereafter. The phenomenon may be related to the loss of c-PBC/ZF in the reactor, the structural destruction of c-PBC/ZF and the blocking of the binding sites with metal complexes (Huang and Liu 2013). The adsorption efficiency of c-PBC/ZF was still close to 90 after six cycles of analysis. Nevertheless, a relatively high adsorption capacity of 35.14 mg/g can be also maintained after six adsorption–desorption cycles. Obviously, the removal efficiency of Th(VI) by c-PBC/ZF did not decrease significantly after six cycles and the slight decrease in the adsorption rate was probably because citric acid dissolves trace amounts of Zn^{2+} and Fe^{3+} in ZF during the analytical process. In addition, it could be easily separated from solutions with magnetic fields after adsorption or desorption because of its superparamagnetism. Therefore, c-PBC/ZF exhibited good regeneration performance and reusability, which can support the long-term utilization of sewage treatment and realize the recovery of radionuclide Th(IV) in wastewater.

Conclusion

Magnetic c-PBC/ZF was successfully synthesized by a hydrothermal method. In the hydrothermal synthesis process, the addition of NTA successfully incorporated abundant carboxyl groups into c-PBC/ZF, which improved the complexing ability between c-PBC/ZF and Th(IV), resulting in its larger adsorption capacity. Characterization results confirmed that ZF materials had been successfully embedded into PBC substrates. It was found that c-PBC/ZF had excellent adsorption properties and a high adsorption rate for Th(IV) by studying the adsorption capacity of c-PBC/ZF to Th(IV) in aqueous solution. The results of adsorption experiments showed that the adsorption process of Th(IV) in solution is related to pH. Th(IV) has a maximum adsorption capacity of 41.47 mg/g at 25 °C, pH = 4.0 and solution concentration of 50 mg/L. The kinetic and isotherm data conformed to the quasi-second-order kinetic and Langmuir isotherm models, respectively. FTIR analysis showed that the c-PBC/ZF removal mechanism of Th(IV) is mainly the formation of Th(IV)-O and carboxyl and hydroxyl complexation with metal ions. Therefore, this study proved that the new synthesis of c-PBC/ZF could effectively remove radioactive Th(IV) as a potential adsorbent in aqueous solution for the further purification of wastewater.

Acknowledgements This work has been partially supported by the Inner Mongolia Natural Science Foundation (2016BS0511,2020MS0 2015,2019LH02006). The authors also thank the anonymous reviewers for their invaluable insight and helpful suggestions.

Compliance with ethical standards

Conflict of interest The authors declare that they have no known competing financial interests or personal relationships that could have appeared to influence the work reported in this paper.

References

Abdelhadi SO, Dosoretz CG, Rytwo G, Gerchman Y, Azaizeh H (2017) Production of biochar from olive mill solid waste for heavy metal removal. Biores Technol 244:759–767

Bhowmik M, Kanmani M, Debnath A, Saha B (2019) Sono-assisted rapid adsorption of anionic dye onto magnetic $CaFe_2O_4$/$MnFe_2O_4$ nanocomposite from aqua matrix. Powder Technol 354:496–504

Dehkhoda AM, Ellis N, Gyenge E (2015) Effect of activated biochar porous structure on the capacitive deionization of NaCl and ZnCl2 solutions. Microporous Mesoporous Mater 224:217–228

dos Santos JMN, Pereira CR, Foletto EL, Dotto GL (2019) Alternative synthesis for $ZnFe_2O_4$/chitosan magnetic particles to remove diclofenac from water by adsorption. Int J Biol Macromol 131:301–308

Ghobadi M, Gharabaghi M, Abdollahi H, Boroumand Z, Moradian M (2018) $MnFe_2O_4$-graphene oxide magnetic nanoparticles as a high-performance adsorbent for rare earth elements: synthesis, isotherms, kinetics, thermodynamics and desorption. J Hazard Mater 351:308–316

Harikishore Kumar Reddy D, Lee S-M (2014) Magnetic biochar composite: facile synthesis, characterization, and application for heavy metal removal. Colloids Surf A 454:96–103

He L, Liu S, Chen L, Dai X, Li J, Zhang M, Ma F, Zhang C, Yang Z, Zhou R (2019) Correction: mechanism unravelling for ultrafast and selective 99TcO4—uptake by a radiation-resistant cationic covalent organic framework: a combined radiological experiment and molecular dynamics simulation study. Chem Sci 10(19):5183–5184

Huang W, Liu ZM (2013) Biosorption of Cd(II)/Pb(II) from aqueous solution by biosurfactant-producing bacteria: isotherm kinetic characteristic and mechanism studies. Colloids Surf B Biointerfaces 105(4):113–119

Huang Z, Li Z, Zheng L, Wu W, Chai Z, Shi W (2019) Adsorption of Eu(III) and Th(IV) on three-dimensional graphene-based macrostructure studied by spectroscopic investigation. Environ Pollut 248:82–89

Huang X, Guida S, Jefferson B, Soares A (2020) Economic evaluation of ion-exchange processes for nutrient removal and recovery from municipal wastewater. npj Clean Water 3(1):7

Jung KW, Lee S, Lee YJ (2017) Synthesis of novel magnesium ferrite ($MgFe_2O_4$)/biochar magnetic composites and its adsorption behavior for phosphate in aqueous solutions. Biores Technol 245:751–759

Kokalj A (2012) On the HSAB based estimate of charge transfer between adsorbates and metal surfaces. Chem Phys 393(1):1–12

Kumar S, Nair RR, Pillai PB, Gupta SN, Sood AK (2014) Graphene oxide-$MnFe_2O_4$ magnetic nanohybrids for efficient removal of lead and arsenic from water. ACS Appl Mater Interfaces 6(20):17426

Li K, Gao Q, Yadavalli G, Shen X, Lei H, Han B, Xia K, Zhou C (2015) Selective adsorption of Gd^{3+} on a magnetically retrievable imprinted chitosan/carbon nanotube composite with high capacity. ACS Appl Mater Interfaces 7(38):21047–21055

Li B, Wang N, Wan J, Xiong S, Liu H, Li S, Zhao R (2016) In-situ gamma-ray survey of rare-earth tailings dams—a case study

in Baotou and Bayan Obo Districts, China. J Environ Radioact 151:304–310

Liang P-L, Yuan L-Y, Deng H, Wang X-C, Wang L, Li Z-J, Luo S-Z, Shi W-Q (2020) Photocatalytic reduction of uranium(VI) by magnetic $ZnFe_2O_4$ under visible light. Appl Catal B 267:118688

Liu J, Zeng M, Yu R (2016) Surfactant-free synthesis of octahedral ZnO/$ZnFe_2O_4$ heterostructure with ultrahigh and selective adsorption capacity of malachite green. Sci Rep 6(1):25074–25074

Mahmed N, Heczko O, Lancok A, Hannula SP (2014) The magnetic and oxidation behavior of bare and silica-coated iron oxide nanoparticles synthesized by reverse co-precipitation of ferrous ion (Fe^{2+}) in ambient atmosphere. J Magn Magn Mater 353:15–22

Marcela S, Cornelia M et al (2015) Fine $MnFe_2O_4$ nanoparticles for potential environmental applications. J Therm Anal Calorim 121(123):1003–1010

Mohammadi M, Sedighi M, Hemati M (2020) Removal of petroleum asphaltenes by improved activity of NiO nanoparticles supported on green AlPO-5 zeolite: process optimization and adsorption isotherm. Petroleum 6(2):182–188

Oter C, Zorer OS (2020) Kinetic, isothermal and thermodynamic studies on Th(IV) adsorption by different modified activated carbons. J Radioanal Nucl Chem 323(1):341–351

Park CM, Kim YM, Kim K-H, Wang D, Su C, Yoon Y (2019) Potential utility of graphene-based nano spinel ferrites as adsorbent and photocatalyst for removing organic/inorganic contaminants from aqueous solutions: a mini review. Chemosphere 221:392–402

Perreault LL, Giret S, Gagnon M, Florek J, Lariviere D, Kleitz F (2017) Functionalization of mesoporous carbon materials for selective separation of lanthanides under acidic conditions. ACS Appl Mater Interfaces 9(13):12003–12012

Shen J, Ma G, Zhang J, Quan W, Li L (2015) Facile fabrication of magnetic reduced graphene oxide-$ZnFe_2O_4$ composites with enhanced adsorption and photocatalytic activity. Appl Surf Sci 359(DEC.30):455–468

Somvanshi SB, Khedkar MV, Kharat PB, Jadhav KM (2020) Influential diamagnetic magnesium (Mg^{2+}) ion substitution in nano-spinel zinc ferrite ($ZnFe_2O_4$): thermal, structural, spectral, optical and physisorption analysis. Ceram Int 46(7):8640–8650

Sun S (2006) Recent advances in chemical synthesis, self-assembly, and applications of FePt nanoparticles. Adv Mater 18(4):393–403

Sun Q, Aguila B, Earl LD, Abney CW, Wojtas L, Thallapally PK, Ma S (2018) Covalent organic frameworks as a decorating platform for utilization and affinity enhancement of chelating sites for radionuclide sequestration. Adv Mater 30(20):1705479

Vergis BR, Kottam N, Hari Krishna R, Nagabhushana BM (2019) Removal of Evans Blue dye from aqueous solution using magnetic spinel $ZnFe_2O_4$ nanomaterial: adsorption isotherms and kinetics. Nano Struct Nano Objects 18:100290

Wang X, Chen L, Wang L, Fan Q, Pan D, Li J, Chi F, Xie Y, Yu S, Xiao C, Luo F, Wang J, Wang X, Chen C, Wu W, Shi W, Wang S, Wang X (2019) Synthesis of novel nanomaterials and their application in efficient removal of radionuclides. Sci China Chem 62(8):933–967

Wang X, Feng J, Zhang Z, Zeng W, Gao M, Lv Y, Wei T, Ren Y, Fan Z (2020) Pt enhanced the photo-Fenton activity of $ZnFe_2O_4$/α-Fe_2O_3 heterostructure synthesized via one-step hydrothermal method. J Colloid Interface Sci 561:793–800

Xiong XH, Yu ZW, Gong LL, Tao Y, Gao Z, Wang L, Yin WH, Yang LX, Luo F (2019) Ammoniating covalent organic framework (COF) for high-performance and selective extraction of toxic and radioactive uranium ions. Adv Sci 6(16):1900547

Xu J, Zhou L, Jia Y, Liu Z, Adesina AA (2015) Adsorption of thorium (IV) ions from aqueous solution by magnetic chitosan resins modified with triethylene-tetramine. J Radioanal Nucl Chem 303(1):347–356

Yang Y, Liu J, Zhang B, Liu F (2017) Mechanistic studies of mercury adsorption and oxidation by oxygen over spinel-type $MnFe_2O_4$. J Hazard Mater 321:154–161

Yezi H, Chaofeng Z et al (2018) Combining batch technique with theoretical calculation studies to analyze the highly efficient enrichment of U(VI) and Eu(III) on magnetic $MnFe_2O_4$ nanocubes. Chem Eng J 349:347–357

Zhang Y, Yan L, Xu W, Guo X, Cui L, Gao L, Wei Q, Du B (2014) Adsorption of Pb(II) and Hg(II) from aqueous solution using magnetic $CoFe_2O_4$-reduced graphene oxide. J Mol Liq 191:177–182

Zhang C, Li X, Chen Z, Wen T, Huang S, Hayat T, Alsaedi A, Wang X (2018) Synthesis of ordered mesoporous carbonaceous materials and their highly efficient capture of uranium from solutions. Sci China Chem 61(3):281–293

Zhang L, Guo J, Huang X, Wang W, Sun P, Li Y, Han J (2019) Functionalized biochar-supported magnetic $MnFe_2O_4$ nanocomposite for the removal of Pb(ii) and Cd(ii). RSC Adv 9:365–376

Zhang Yakun Yan Liangguo XW (2014) Adsorption of Pb(II) and Hg(II) from aqueous solution using magnetic $CoFe_2O_4$—reduced graphene oxide. J Mol Liq 191(193):177–182

Zhu S, Ho SH, Huang X, Wang D, Yang F, Wang L, Wang C, Cao X, Ma F (2017) Magnetic nanoscale zerovalent iron assisted biochar: interfacial chemical behaviors and heavy metals remediation performance. ACS Sustain Chem Eng 5(11):9673–9682